

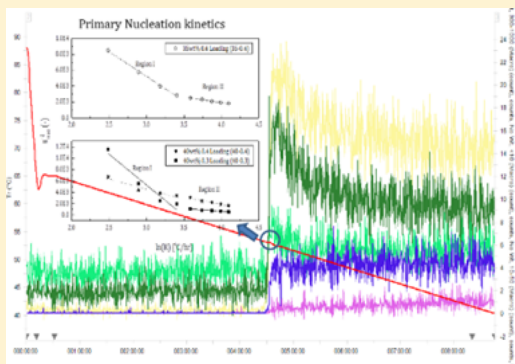
Precipitating Characteristics of Potassium Bicarbonate Using Concentrated Potassium Carbonate Solvent for Carbon Dioxide Capture. Part 1. Nucleation

Yue Wu, Nouman R. Mirza, Guoping Hu,^{iD} Kathryn H. Smith,^{iD} Geoffrey W. Stevens,^{iD} and Kathryn A. Mumford^{*ID}

Department of Chemical and Biomolecular Engineering, The University of Melbourne, Victoria, Australia

Peter Cook Centre for CCS Research, The University of Melbourne, Victoria, Australia

ABSTRACT: Potassium carbonate is considered a promising solvent for carbon dioxide (CO_2) capture as it is cost-effective and environmentally benign when compared to traditional amine-based solvents. In order to increase absorption capacity, the use of concentrated potassium carbonate solvent has been proposed in which CO_2 absorption results in precipitation of bicarbonate. Understanding the formation of the solids in that system is important if this is to be used for CO_2 capture. In this work, the precipitation behavior in the ternary system of potassium carbonate–potassium bicarbonate–water was studied in a batch cooling crystallizer equipped with Focused Beam Reflectance Measurement (FBRM) and an Optimax workstation. The solubility data were validated using a regressed Electrolyte Non-Random Two Liquid (ENRTL) activity model developed in Aspen Plus. The precipitate was determined as kalicinite with hexagonal prism shape by X-ray Diffraction (XRD) and Scanning Electron Microscopy (SEM). The nucleation kinetics were evaluated using the metastable zone width method and induction time method. Results indicated that in the studied ternary system there were two separate regions corresponding to different nucleation mechanisms, which were defined by the cooling rate. The supersaturation of potassium bicarbonate and the concentration of potassium carbonate determined the nucleation kinetics. On the basis of the calculated nucleation kinetics, the continuous growth mechanism of the crystals was further examined using the surface entropy value and SEM images.

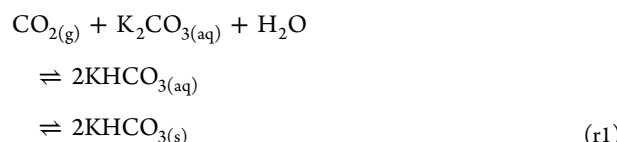


1. INTRODUCTION

Carbon capture and storage is a promising way to reduce greenhouse gas emissions, particularly from industrial sources such as coal-fired power plants, cement manufacture and other chemical processes. Traditional fossil fuels are still used as primary energy resources, and their use is expected to continue to rise until 2030 and beyond.^{1,2} Among the different carbon capture technologies, solvent-based chemical absorption is currently the most feasible and mature technology available.² Compared to conventional amine solvents used in carbon capture, potassium carbonate (K_2CO_3) solvent has gained interest recently as it is environmentally benign, less toxic, less likely to cause problems associated with degradation, and less corrosive.^{3–5} K_2CO_3 solvent absorption, however, has two challenges to be addressed: (1) improvement in the absorption efficiency via introduction of various promoters to accelerate CO_2 reaction kinetics⁶ and (2) improvement in the absorption capacity through the precipitation, or phase change, of the absorbed CO_2 containing species.^{7,8}

When carbon dioxide (CO_2) is absorbed continuously into concentrated K_2CO_3 solvent, the product, potassium bicarbonate (KHCO_3), will eventually precipitate out as the solubility limit is reached. This reaction is shown in reaction

r1, and according to Le Chatelier's principle, the equilibrium can be shifted to the right by removing KHCO_3 as it precipitates, thus improving the absorption capacity. Therefore, investigation of precipitation behavior, including nucleation and growth kinetics of KHCO_3 , becomes important for large scale design and implementation of this precipitating solvent absorption process. The aim of this study is to investigate the nucleation behavior of KHCO_3 in the $\text{KHCO}_3\text{--K}_2\text{CO}_3\text{--water}$ ternary system, which will provide guidelines and insights into using concentrated K_2CO_3 solvent for CO_2 capture.



Nucleation involved in crystallization can be detected and measured easily and accurately in a batch crystallizer using

Received: February 20, 2017

Revised: May 5, 2017

Accepted: May 24, 2017

Published: May 24, 2017

precise temperature control strategies, where the nucleation is detected through a number of *in situ* process analytical techniques (PAT) such as turbidity,^{9–11} ultrasonic technology,^{11,12} electrical conductivity,¹³ imaging techniques,^{14,15} and focused beam reflectance measurement (FBRM).^{14,16–19} Unlike off-line measurements, these *in situ* and online techniques avoid interruption to the crystallization process to a large extent, which in turn increases the sensitivity and reliability of detecting the nucleus. FBRM has recently gained more interest as it can directly track the size and number of particles in terms of chord length distribution throughout the crystallization process, and it is also reliable and sensitive enough to be able to detect small particles related to nucleation which are approximately 10 μm in size. In this study, concentrated K₂CO₃ solvent with different KHCO₃ compositions was used to measure the metastable zone width and induction time of KHCO₃ precipitation. These data were collected using an unseeded batch crystallizer through FBRM (Mettler Toledo) with accurate temperature control from an Optimax workstation (Mettler Toledo). The nucleation kinetics were analyzed using the experimental data.

2. THEORETICAL APPROACHES FOR EVALUATING NUCLEATION KINETICS

Generally, there are two steps involved in the crystallization process: nucleation and crystal growth. Supersaturation, which is defined as the amount that the measured concentration of solute exceeds its saturated concentration (thermodynamic solubility) at a certain temperature, is the primary driving force for both crystal nucleation and growth. Therefore, measuring the real-time concentration and solubility of the solute are essential for evaluating nucleation kinetics accurately.

Solubility is a thermodynamic property which depends on the concentration of the solute and temperature. In a batch process, the solubility can be measured using either the thermal equilibrium method or the thermal dynamic method. For the thermal equilibrium method, the suspension is kept at a constant temperature for sufficient time to ensure it reaches thermal equilibrium, and the concentration of the supernatant is the saturated concentration at this specific temperature. For the thermal dynamic method, a known concentration of the suspension is heated up using a very low heating rate to ensure that the solution is at thermal equilibrium at all times. The temperature at the point that the last particle is dissolved is the saturated temperature for the measured concentration of solution. In this study, both methods were used to measure the solubility of KHCO₃ in the KHCO₃–K₂CO₃–water ternary system.

Two methods may be used to generate supersaturation using temperature control in a batch crystallization process, these are the metastable zone width (MSZW) method and induction time method. The MSZW method is based on a polythermal technique, whereas the induction time method depends on an isothermal technique. The MSZW method has been widely used.^{20–23} In this method, the nucleation rate J is related to the supersaturation S which is generated via altering the temperature within the crystallizer. When the temperature is reduced such that the KHCO₃ concentration reaches its solubility, nucleation does not occur spontaneously, rather it occurs when it reaches the supersolubility. Therefore, the MSZW is defined as the gap between the supersolubility and solubility curves. The supersaturation expressions commonly used include the

absolute supersaturation ΔC , relative supersaturation σ , and supersaturation ratio S , which are defined in eqs 1–3.²⁴

$$\Delta C = C - C^* \quad (1)$$

$$\sigma = \frac{\Delta C}{C^*} = \frac{C - C^*}{C^*} \quad (2)$$

$$S = \frac{C}{C^*} \quad (3)$$

where C is real-time concentration (mol·m⁻³) and C^* is saturation concentration (mol·m⁻³). In order to evaluate nucleation kinetics effectively, the constant cooling rate proposed by Mersmann²⁴ is normally applied to the MSZW method, which will be detailed in section 3.3. On the basis of the constant cooling rate, three approaches are given to interpret the MSZW in this study: Nývlt approach, Self-consistent Nývlt approach and Sangwal's classical nucleation approach.

2.1. Nývlt Approach. Nývlt's equation was first used to explain the MSZW by assuming a "pseudo" steady state during a limited time from the onset of nucleation. This represents the change in supersaturation with a change in temperature corresponding to a change in solubility at a specific temperature. This relationship is shown by eq 4,²⁵ where T is the temperature (K).

$$\frac{\Delta C}{\Delta T} = \left(\frac{dC^*}{dT} \right)_T \quad (4)$$

Within the time region, the nucleation rate J (#·m⁻³·s⁻¹) can be described both as an empirical power-law equation and as a classical nucleation theory with a constant cooling rate $R = \Delta T/\Delta t$, where # is the total number of particles and t is the time (h). The expressions are indicated in eqs 5 and 6, respectively.²⁶

$$J = k(\Delta C)^m \quad (5)$$

$$J = \left(\frac{dC^*}{dT} \right)_T R \quad (6)$$

where k is the apparent nucleation rate constant (#·mol^{-m}·m^{3m-3}·s⁻¹) and m is the apparent nucleation order.

At the boundary of the MSZW, the supersaturation ΔC is replaced by ΔC_{\max} corresponding to the maximum temperature width ΔT_{\max} , which is the difference between the temperature at supersolubility curve T_{\max} and the temperature at solubility curve T^* . Combining eq 4 with eq 6 and taking the logarithm on both sides, a linear relationship between $\ln T_{\max}$ and $\ln R$ is obtained as shown in eq 7.

$$\ln \Delta T_{\max} = \frac{1-m}{m} \ln \left(\frac{dC^*}{dT} \right)_T - \frac{1}{m} \ln k + \frac{1}{m} \ln R \quad (7)$$

ΔT_{\max} can be measured from a series of data with constant cooling rate R , and $\left(\frac{dC^*}{dT} \right)_T$ can be assessed from the measured solubility curve. The nucleation parameters k and m are then evaluated from the linear relationship.

Although Nývlt's equation may be fitted with extensive MSZW experiments well, the physical interpretation of k and m is unclear, especially when introducing impurities and seeds.^{21,23}

2.2. Self-Consistent Nývlt Approach. To simplify the complicated unit of the nucleation rate constant k in Nývlt's

equation, Sangwal proposed a self-consistent Nývlt approach by introducing the supersaturation ratio S_{\max} instead of absolute supersaturation ΔC_{\max} . Equation 5 is replaced by eq 8, and now k has the same unit as the nucleation rate J ($\#\cdot m^{-3}\cdot s^{-1}$).²⁷

$$J = k(\ln S_{\max})^m \quad (8)$$

Using the assumption of regular solutions,²⁷ $\ln S_{\max} \approx \sigma_{\max}$ the relationship between S_{\max} and ΔT_{\max} may be described by eq 9.

$$\ln S_{\max} = \sigma_{\max} = \frac{\Delta H_s}{R_{\text{gas}}T^*} \cdot \frac{\Delta T_{\max}}{T_{\max}} = \frac{\lambda u_{\max}}{1 - u_{\max}} \quad (9)$$

where ΔH_s is the enthalpy of dissolution ($J\cdot mol^{-1}$), R_{gas} is gas constant ($8.3145 J\cdot mol^{-1}\cdot K^{-1}$), T^* is saturation temperature (K), T_{\max} is nucleation temperature (K), $\lambda = \Delta H_s/R_{\text{gas}}T^*$, and $u_{\max} = \Delta T_{\max}/T^*$.

Additionally, nucleation rate, J , is a function of the change of the supersaturation changing with time, which can be described as eq 10.

$$J = \frac{f\sigma_{\max}}{\Delta t} = f \cdot \frac{\lambda u_{\max}}{1 - u_{\max}} \cdot \frac{1}{\Delta t} = f \cdot \left(\frac{\lambda u_{\max}}{1 - u_{\max}} \right) \cdot \frac{1}{\Delta T_{\max}}. \\ \frac{\Delta T_{\max}}{\Delta t} = f \cdot \left(\frac{\lambda}{1 - u_{\max}} \right) \left(\frac{R}{T^*} \right) \quad (10)$$

where f is a proportionality constant ($\#\cdot m^{-3}$), which may be estimated from the saturation concentration of the solute.

By substituting eq 9 into eq 8, and combining with eq 10, a linear logarithmic relationship between u_{\max} and R can be obtained, as shown by eq 11:

$$\ln u_{\max} = \varphi + \beta \ln R \quad (11)$$

Where,

$$\varphi = \frac{1-m}{m} \ln \left(\frac{\lambda}{1 - u_{\max}} \right) + \frac{1}{m} \ln \left(\frac{f}{kT^*} \right) \quad (12)$$

$$\beta = \frac{1}{m} \quad (13)$$

Through the self-consistent Nývlt approach, the redefined nucleation rate constant k and nucleation order m can be obtained from the interception and slope of the plot based on eq 11.

2.3. Sangwal Approach with Classical Nucleation Theory (CNT). Although the unit of redefined nucleation rate constant k is simplified by using the self-consistent Nývlt approach, the physical meaning of parameters k and m is still obscure.²³ Sangwal developed a new approach using classical three-dimensional nucleation theory (CNT).²⁷ The CNT is deduced from the condensation of a water droplet based on the free Gibbs energy,²⁸ and the nucleation rate J is given by eqs 14 and 15.²⁹

$$J = A \exp \left(-\frac{B}{\ln^2 S_{\max}} \right) \quad (14)$$

with

$$B = \frac{16\pi}{3} \cdot \left(\frac{\gamma_{\text{eff}} \Omega^{2/3}}{T_{\max} \kappa_B} \right)^3 = \frac{16\pi}{3} \cdot \left(\frac{\omega}{1 - u_{\max}} \right)^3 \quad (15)$$

where A is the pre-exponential kinetic constant ($\#\cdot m^{-3}\cdot s^{-1}$), γ_{eff} is effective liquid–solid interfacial energy ($J\cdot mol^{-1}$), Ω is molecular volume (m^3), κ_B is the Boltzamann constant ($J\cdot mol^{-1}\cdot K^{-1}$), and ω defined as eq 16.

$$\omega = \frac{\gamma_{\text{eff}} \Omega^{2/3}}{T^* \kappa_B} \quad (16)$$

Substituting eq 9 into eq 14, and combining with eq 15 and eq 10, a new expression is obtained as shown by eq 17.

$$\exp \left[-\frac{16\pi}{3} \cdot \frac{\omega^3}{\lambda^2 (1 - u_{\max}) u_{\max}^2} \right] = f \cdot \left(\frac{\lambda}{1 - u_{\max}} \right) \left(\frac{R}{AT^*} \right) \quad (17)$$

Upon rearrangement and taking the logarithm of eq 17, a linear relation of u_{\max}^{-2} and $\ln R$ may be obtained, which is indicated in eq 18.

$$\frac{1}{(1 - u_{\max}) u_{\max}^2} \approx u_{\max}^{-2} = F_1 [-\ln R + X + \ln T^*] \\ = F - F_1 \ln R \quad (18)$$

where

$$F = F_1 (X + \ln T^*) \quad (19)$$

$$F_1 = \frac{1}{B} \cdot \left(\frac{\Delta H_s}{R_{\text{gas}} T_{\max}} \right)^2 \quad (20)$$

$$X = \ln \left(\frac{A}{f} \cdot \frac{R_{\text{gas}} T_{\max}}{\Delta H_s} \right) \quad (21)$$

On the basis of classical nucleation theory (eq 14), the slope of the resulting plot F_1 (eq 18) is inversely related to the nucleation thermodynamic constant B (eq 20), while the intercept F in eq 18 is related to both the thermodynamic constant B (eq 20) and the nucleation kinetic constant A (eq 21).

2.4. Theoretical Interpretations of Induction Time.

Although the three approaches described may be used to interpret the MSZW, they do not provide any insight about induction time, which is another important characteristic related to nucleation kinetics.²³ The isothermal method is usually used for measuring the induction time for a batch crystallizer. The prepared solution at known concentration is heated approximately 5 °C above its saturation temperature and then cooled down to the preset temperature at the maximum cooling rate that the instrument allows. Therefore, the induction time, t_{ind} , is defined as the time elapsed between the first detectable nuclei and the time when reaching the preset temperature, which is shown by eq 22.

$$t_{\text{ind}} = \frac{1}{J} \quad (22)$$

Upon combination of eq 22 with the classical nucleation theory represented by eq 14, a relationship between the induction time and nucleation kinetics represented by eq 23 may be formed.

$$\begin{aligned}\ln t_{\text{ind}} &= -\ln A + \frac{B}{\ln^2 S_{\max}} \\ &= -\ln A + \left[\frac{16\pi}{3} \cdot \left(\frac{\gamma_{\text{eff}}^3 \Omega^2}{T_{\max}^3 k_B^3 \ln^2 S_{\max}} \right) \right] \quad (23)\end{aligned}$$

where the symbols have the same meaning as defined previously.

A number of studies have been published on the induction time method.^{18,19,22,30} By adopting a polythermal method with a constant cooling rate, the similarly named “pseudo” induction time can be measured in this study, which is discussed in detail in section 3.3.

3. EXPERIMENTS

3.1. Chemicals and Instruments. Potassium carbonate ($\geq 99.5\%$, UNID) and potassium bicarbonate ($> 98\%$, Consolidated Chemical Co.) were used without further treatment. Ultrapure water ($18.2 \text{ M}\Omega\text{-cm}^{-1}$, Elix Milipore) was used to prepare all solutions. Sulfuric acid (98%, Science Supply) was used and diluted to titrate the concentration of potassium carbonate and potassium bicarbonate.

An Optimax 1001 workstation (Mettler Toledo, CH) integrated with precise temperature control and stirring speed control was used for the series of experiments. Temperature control was achieved from a feedback control with an external water bath (WKL 2200, LAUDA), and a stainless steel stirrer with four blades at a pitch of 45° was used for agitation, which was controlled through an overhead motor connected to Optimax. The FBRM probe G400 (Mettler Toledo, CH), which communicated with Optimax, was used for detecting nucleation.

A Metrohm 905 Titrando autotitrator (CH) was used for determining the concentration of K_2CO_3 and KHCO_3 in the solution. Nucleation samples were qualified by off-line techniques including X-ray Diffraction (XRD, Bruker D2 Phaser) and Field Emission Scanning Electron Microscopy (FESEM, Philips XL30 FEG, 2 kV beam).

3.2. Solubility Measurement. The solubility of KHCO_3 in the prepared K_2CO_3 – KHCO_3 – H_2O ternary solution system was measured at thermal equilibrium in Optimax. The solution was heated up to 85°C with agitation of 400 rotations per minute (RPM) and kept at this temperature for 20 min in a closed crystallizer to ensure all the solids were dissolved and no gas was generated. The solution was then cooled down to several preset temperatures ranging from 20 to 60°C , which were similar to industrial absorber operating conditions, and kept constant at each temperature for 90 min to ensure both solid and liquid were in equilibrium. The stirrer was then stopped, and 30 min was allowed for the solids to settle to the bottom of the crystallizer. Three parallel groups of clear supernatant were withdrawn using a 2 mL pipet.

Samples were titrated using the Metrohm 905 Titrando autotitrator.^{31,32} A total of 2 mL of each sample was first diluted with ultrapure water and then titrated using 0.4 M sulfuric acid based on end-point pK_a values of CO_3^{2-} and HCO_3^- concentrations, which were 10.33 and 6.37, respectively. To check if there were small particles suspending in the clear supernatant, a number of supernatants were also withdrawn and immediately put into a centrifuge with temperature control under 2000 rpm for 2 min and then titrated using the same method.

Moreover, in order to confirm the reliability of the thermal equilibrium method used for measuring solubility, an extra experiment using the dynamic thermal method was conducted. A known composition of solution was heated at an extremely slow rate of 0.05 K/min from room temperature, and the temperature at which the last particle dissolved was considered the solubility temperature corresponding to the known concentration of the solution.

3.3. Nucleation Measurement. Previous researchers have found that to effectively operate a solvent absorption CO_2 capture system, the required CO_2 loading of apparent concentrated K_2CO_3 solution (35 wt % to 40 wt %) is 0.3 to 0.4 based on vapor–liquid equilibrium data.³³ Here, the CO_2 loading is defined as moles of CO_2 absorbed by the K_2CO_3 solution, which can be calculated as $[\text{HCO}_3^-]/[\text{K}^+]$.³⁴ The apparent K_2CO_3 concentration is based on the assumption that pure K_2CO_3 is used initially, which means KHCO_3 formed from the absorption of CO_2 is converted to initial K_2CO_3 concentration. From this, a group of experiments was designed to investigate nucleation kinetics, as shown in Table 1.

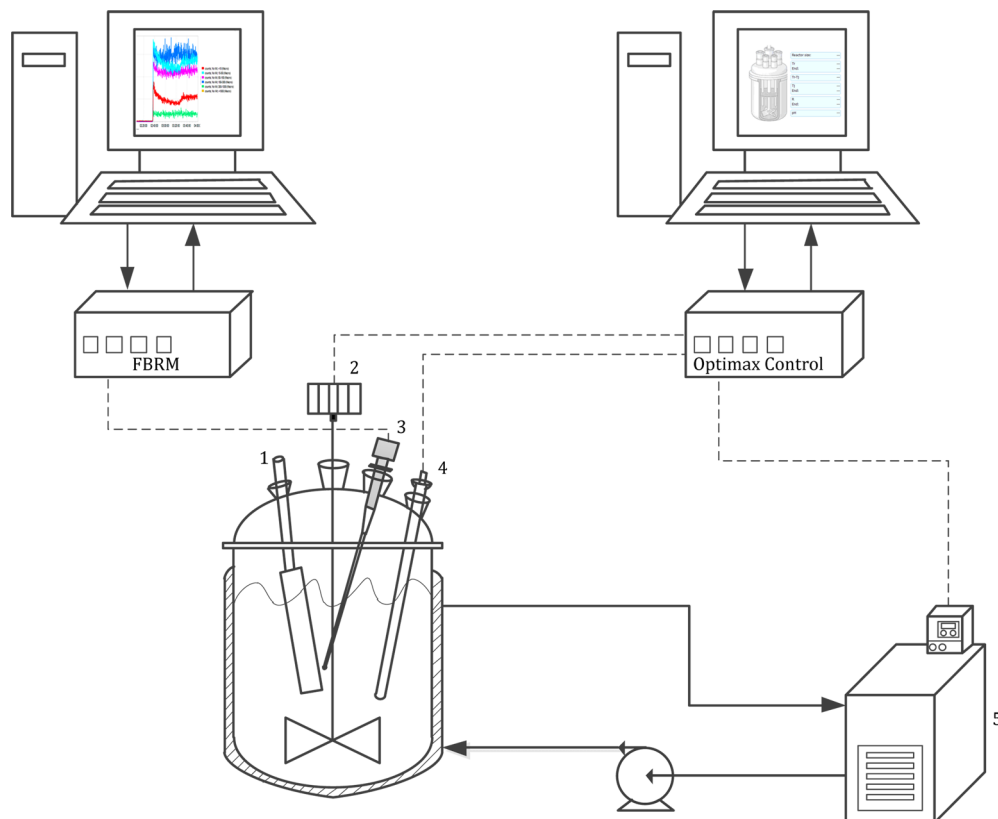
Table 1. Experimental Design for Nucleation Kinetics

experiment group	apparent K_2CO_3 concentration (wt %)	CO_2 loading (–)	constant cooling rate ($^\circ\text{C}/\text{min}$)	interval ($^\circ\text{C}/\text{min}$)
40–0.4	40	0.4	0.1 to 1	0.1
35–0.4	35	0.4	0.1 to 1	0.1
40–0.3	40	0.3	0.1 to 1	0.1

FBRM is based on intensive laser backscattering technology. The focused beam is transmitted into the solution along the center of the probe through a rotary sapphire window. When the laser beam contacts both sides of the particle, the laser is backscattered to the receptor in sequence. The time elapsed between these two signals is transformed in terms of chord length representing the size of the particle.³⁵ In this study, the scan speed of FBRM was set as $2 \text{ m}\cdot\text{s}^{-1}$, and the scan interval was 10 s. The FBRM was positioned at a 45° inclination with the baffle blade to increase the detectable sensitivity, and testing mode was selected as “Macro” due to the transparent surface of the crystals.

To reduce the stochastic nature of the onset of nucleation, a large glass crystallizer with a volume of 1 L was selected.³⁶ The crystallizer was controlled by Optimax, and FBRM communicating with Optimax through iC control (version 5.4), and iC FBRM (version 4.3.2) software was used for detecting the nuclei. The schematic is shown in Figure 1.

The prepared solutions shown in Table 1 were heated up to 85°C to ensure that all the solids were dissolved, and three samples were taken out to obtain initial concentration using the same titration method as described for measuring solubility. The solution was cooled down to 65°C and maintained for 30 min. Further cooling was conducted at a preset rate until the end temperature of 25°C was reached, and this was maintained for another 30 min. The nucleation temperature corresponds to the temperature at which the chord length increased above $10 \mu\text{m}$ with a sharp increase as measured by the FBRM. Each cooling rate experiment was repeated three times. The effect of agitation rate (200, 300, 400, 500, and 600 rpm) on nucleation in experiment 40–0.4 (shown in Table 1) at a constant cooling rate of 0.05 K/min was also investigated.



1 – Baffle blade, 2 – Impeller, 3 – FBRM, 4 – Temperature sensor, 5 – Water bath

Figure 1. Nucleation measurement flowchart using Optimax and FBRM.

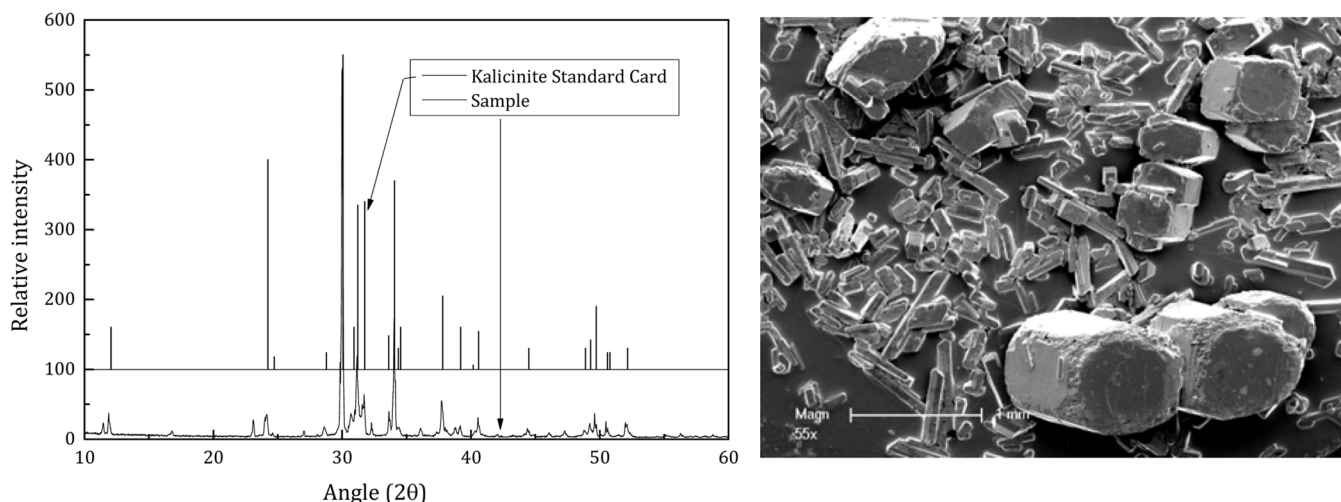


Figure 2. Typical XRD and SEM results for the nucleation sample from experiment 40–0.3.

Rather than the traditional isothermal method for measuring induction time, a “pseudo” induction time was used which is based on the cooling experiments using a polythermal method.²³ Here, “pseudo” induction time was defined as the time elapsed between the saturation temperature which was measured from the solubility curve and the nucleation temperature at which FBRM detected the first nuclei during the cooling process. Therefore, eq 23 can be rewritten as eq 24 and then used to determine nucleation kinetics.

$$\ln t_{\text{ind}} = \ln \left(\frac{\Delta T_{\max}}{R} \right) = -\ln A + \left[\frac{16\pi}{3} \cdot \left(\frac{\gamma_{\text{eff}}^3 \Omega^2}{T_{\max}^3 K_B^3 \ln^2 S_{\max}} \right) \right] \quad (24)$$

4. RESULTS AND DISCUSSION

4.1. Precipitate Qualification. The crystals that precipitated from the ternary system were qualified through off-line XRD and SEM analysis. When the experiment was finished, the suspension was discharged and immediately filtered. The solids

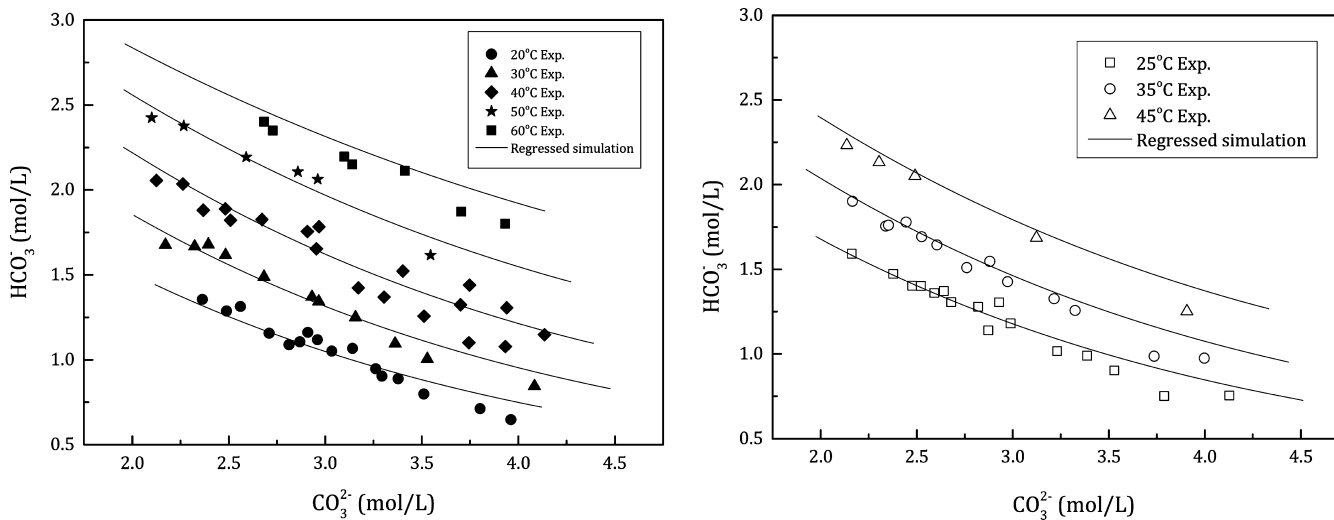


Figure 3. Experimental data determined in this work and solubility curve for the $\text{K}_2\text{CO}_3-\text{KHCO}_3-\text{H}_2\text{O}$ system predicted from Lee and Mumford.³⁹

were then washed using ethanol (100%, chem-supply) and dried in a vacuum drier. The dried sample was analyzed through XRD, using Cu-K α ($\lambda = 0.15406 \text{ nm}$) radiation (40 kV, 40 mA). The diffraction peaks were collected by scanning the sample from 5° to 60° with a step-scan width of 0.05° and a scan speed of $0.5^\circ/\text{min}$. Also, the dried samples were placed onto aluminum stubs using carbon tabs and gold coated using an Edward S150B sputter coater for the purpose of imaging in SEM.³⁷ Both the XRD result and the SEM result are shown in Figure 2.

Compared to the standard XRD for KHCO₃, K₂CO₃, and K₂CO₃·1.5H₂O, kalicinite (KHCO₃) was the only precipitate in the ternary system, although there were some unmatched peaks due to the presence of impurities. The crystals were also found to have a uniform shape of a hexagonal prism, and the results agreed with the results of Lu et al.,³⁸ who have also presented data for bicarbonate crystallization.

4.2. Solubility. In the experiment described in section 3.2, the solution was allowed to sit for 30 min before a sample was collected to allow all the solids to settle. Experiments were also conducted with centrifugation after this 30 min settling time, and the titration results were the same for samples without centrifugation, indicating that 30 min is sufficient time for the solids to settle.

The Electrolyte Nonrandom Two Liquid (ENRTL) model was used in this study to validate experimental solubility data in the KHCO₃-K₂CO₃-H₂O ternary system. This thermodynamic model was used in our previous studies with K₂CO₃ solvent after being regressed using nearly 3000 experimental data points with the Data Regress System (DRS) in Aspen Plus. The solubility calculated in the model was based on the activity of each electrolyte; further detail on the model can be found in Lee and Mumford's work.³⁹ Solubility results from both the model and the experiments are shown in Figure 3.

The experimental data fitted the predicted results well (within $\pm 4.2\%$) except for some points at high concentrations of CO₃²⁻. The concentration of HCO₃⁻ seemed to be slightly underestimated at higher CO₃²⁻ concentrations (above 3.5 mol/L CO₃²⁻ concentration) most likely due to the lack of data at higher concentrations used for regression of the ENRTL model. However, as only a 35 to 40 wt % apparent K₂CO₃ concentration with a loading ranging from 0.3 to 0.4 was used in this study, which corresponds to a 2 to 2.5 mol/L CO₃²⁻

concentration, the fit is considered acceptable for use in the model to simulate the solubility of the ternary system used in these experiments.

4.3. Metastable Zone Width Analysis. Experiments were conducted using the plan presented in Table 1. The nucleation temperatures for different apparent K₂CO₃ concentrations and CO₂ loadings are shown in Figure 4.

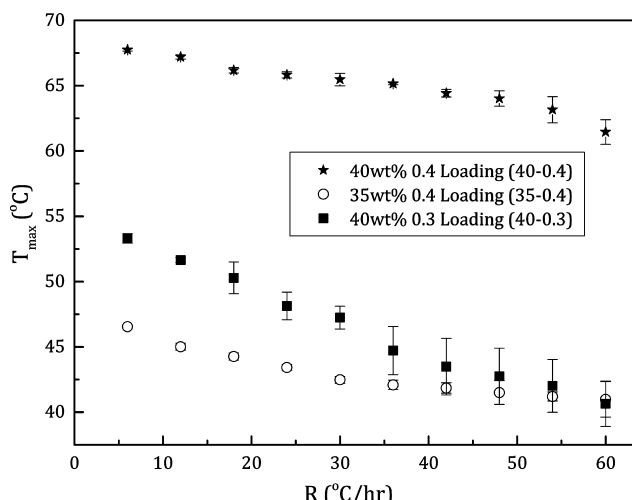


Figure 4. Nucleation temperatures of the ternary system with different loadings and solvent concentrations.

The nucleation temperature of the ternary system depended on both the concentration of KHCO₃ (loading) and the concentration of K₂CO₃ (apparent K₂CO₃ concentration). All experiments showed a trend of nucleation temperatures decreasing with increasing cooling rate, which means the metastable zone widened at higher cooling rates. This is because the time required to form a detectable nucleus at higher cooling rates was delayed, while the slow change of the temperature ensured the formation of clusters could respond.⁴⁰ This trend is consistent with a number of published works.^{19,41,42} In addition, it was found at higher cooling rates that the deviation became larger due to the stochastic nature of nucleation at high supersaturation.

The effect of agitation on the MSZW was also investigated, and no general trend could be found. This is probably because of the dual effects of agitation on nucleation. That is, strong agitation promotes turbulence in the solution, increasing mass transfer and opportunities of forming nuclei; however, it also increases the shear force on the crystal nuclei or particles and can break them, resulting in nucleus debris being redissolved in the solution.⁴³

4.3.1. Nývlt Relation. Using eq 7, the linear relationship between MSZW and cooling rate is obtained, as shown in Figure 5. It was found that the concentration of K_2CO_3 did

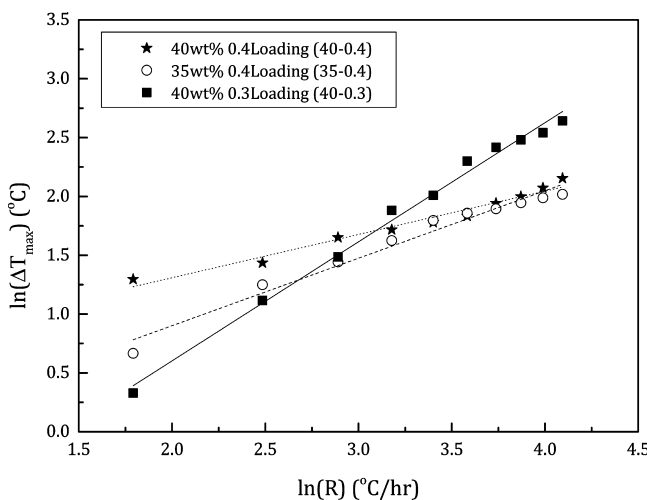


Figure 5. Relationship between ΔT_{\max} and cooling rate using Nývlt's equation.

have an effect on KHCO_3 nucleation. In experiments 40–0.4 and 35–0.4, for example, there was a large difference between the $\ln \Delta T_{\max}$ at low cooling rates. However, as the cooling rates increased, the effect of K_2CO_3 concentration on the nucleation temperature was reduced. In addition, there was an intersection between experiments 40–0.4 and 40–0.3, which was most likely caused by dual effects from electrolyte interactions and supersaturation. Compared to experiment 40–0.3, experiment 40–0.4 had a higher KHCO_3 concentration and higher ionic strength, and nucleation had to overcome the electrolyte interactions between KHCO_3 and K_2CO_3 , thus having a wider MSZW at low cooling rates. While at high cooling rates, supersaturation became the major driving force and dominated the nucleation, as shown by experiment 40–0.4, which had higher supersaturation and a narrower MSZW, leading to a smaller ΔT_{\max} .

From the linear relationship, the nucleation kinetics constants k and m can be evaluated, and results are shown in Table 2. T^* and $\left(\frac{dC^*}{dT}\right)_T$ for each experiment can be obtained from the ENRTL model. Higher nucleation kinetics constant k and nucleation order m results in a higher nucleation rate.

4.3.2. Self-Nývlt Relationship. Using eq 11, the simplified-unit relationship between MSZW and cooling rate can be described by the self-Nývlt equation, which is shown in Figure 6, where $u_{\max} = \Delta T_{\max}/T^*$. A similar linear trend can be found;

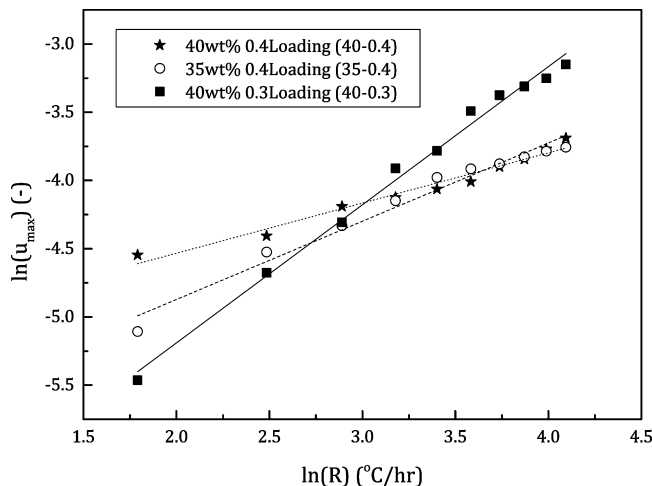


Figure 6. Relationship between U_{\max} and cooling rate using the self-Nývlt equation.

therefore, the parameters of nucleation kinetics can be evaluated, which are shown in Table 3. The enthalpy of dissolution ΔH_s is obtained from the ENRTL model through eq 25.⁴⁴

$$\ln C^* = B_1 - \frac{\Delta H_s}{R_{\text{gas}} T^*} \quad (25)$$

As the self-Nývlt approach using eq 8 is a simplified expression of the Nývlt approach using eq 5, it is not surprising that the nucleation orders obtained from both approaches are the same. However, in the self-Nývlt approach, the nucleation kinetics constant k is dependent on the saturation temperature T^* and nucleation order m , which means the initial composition and mutual interactions between electrolytes are critical to the ternary system.²⁷ This conclusion is justified from the above experiments. With an increase in K_2CO_3 concentration and CO_2 loading, the nucleation kinetics constant k increased.

4.3.3. Sangwal with Classical Nucleation Theory (CNT) Relationship. Using the physically more meaningful CNT method proposed by Sangwal, a new relationship between U_{\max} and cooling rate was obtained, which is shown in Figure 7.

Following the recommendation of Sangwal,⁴⁵ the cooling rate of 0.1 °C/min was excluded from all three groups of experiments, in order to get a linear relationship. Without the lowest cooling rate, it was found that for each combination of apparent K_2CO_3 concentrations and loadings, the results were divided into two linear regions, although experiment 40–0.4 showed an overall linear relationship over the entire cooling

Table 2. Nucleation Kinetics Parameters Obtained Using Nývlt's equation

experiment group	saturation temperature T^* (°C)	$\left(\frac{dC^*}{dT}\right)_T$	slope	intercept	R^2	$k (\# \cdot \text{mol}^{-m} \cdot \text{m}^{3m-3} \cdot \text{s}^{-1})$	m
40–0.4	71.4	0.0358	0.368	0.574	0.97	64.2	2.72
35–0.4	48.5	0.0392	0.574	-0.246	0.97	17.1	1.74
40–0.3	54.7	0.0357	1.01	-1.42	0.99	3.92	0.988

Table 3. Nucleation Kinetics Parameters Obtained Using the Self-Nyvlt Equation

experiment group	ΔH_s (kJ/mol)	f (#/ m^3)	slope β	intercept φ	R^2	k (#· s^{-1})	m
40–0.4	14.9	1.87×10^{27}	0.368	-5.27	0.97	5.14×10^{29}	2.72
35–0.4	15.5	1.57×10^{27}	0.574	-6.02	0.97	4.72×10^{28}	1.74
40–0.3	17.6	1.42×10^{27}	1.01	-7.21	0.99	5.51×10^{27}	0.988

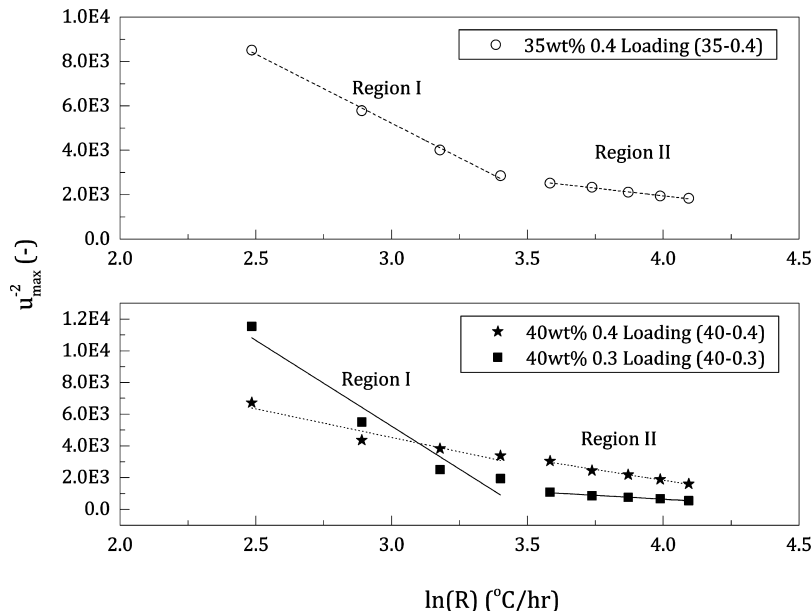


Figure 7. Relationship obtained using Sangwal's approach with CNT.

rate range investigated above 0.1 °C/min. These two linear relationships are a result of homogeneous nucleation occurring at high cooling rates and heterogeneous nucleation occurring at low cooling rates.

The nucleation kinetics parameters, including the pre-exponential kinetic rate constant A and thermodynamic nucleation constant B , were evaluated based on the linear relationships for each region, and the nucleation kinetics parameters from eq 14 are shown in Table 4.

Table 4. Nucleation Kinetics Parameters Obtained Using Sangwal Equation with CNT

experiment group	slope ($-F_{ij}$) $\times 10^{-3}$)	intercept F $\times 10^{-3}$)	R^2	B ($\times 10^3$)	A (# $m^{-3} \cdot s^{-1}$) $\times 10^{-27}$)
40–0.4	region I	3.61	15.4	0.88	7.72
	region II	2.72	12.7	0.98	3.09
35–0.4	region I	6.22	23.9	0.99	5.58
	region II	1.39	7.52	0.99	6.41
40–0.3	region I	10.8	37.7	0.92	4.00
	region II	0.993	4.61	0.97	3.01

The nucleation kinetics constant, A , from the CNT model is determined from experimental data presented in Table 4. Higher cooling rates results in higher supersaturation, thus leading to higher A values and nucleation rates. The different values of B , which represents crystal interfacial interaction, also reflect the observed intersection between experiment 40–0.4 and experiment 40–0.3 shown in Figure 5. This demonstrates that the concentration of KHCO_3 is not the only driving force for the nucleation; K_2CO_3 concentration also has an impact on nucleation. This may be because at low cooling rates, K_2CO_3

has a strong interaction with H_2O and KHCO_3 , thus having a high energy barrier for KHCO_3 nucleation, resulting in a higher value of B and lower nucleation rate in experiment 40–0.4 compared to experiment 40–0.3. However, with the increase of cooling rates, KHCO_3 concentration dominates the nucleation, thus having a lower value of B and higher value of nucleation in experiment 40–0.4 in comparison with experiment 40–0.3.

The two regions are also identified in the FBRM data, which is shown in Figure 8. The two different cooling rates (0.2 °C/min and 0.7 °C/min) represent the two different regions in experiment 40–0.3. As described in the experimental procedures, three parallel experiments were conducted under the same conditions, and all three sets of data are shown in Figure 8. The results showed that there was an obvious difference in all sets of data as shown in the black frame. The nucleation that occurred at 0.7 °C/min (Figure 7, region II) had a second bump in the small particles during the cooling process, whereas a monotonic trend occurred at 0.2 °C/min (Figure 7, region I). This difference was observed and repeated at all ranges of cooling rates, indicating that there are two nucleation mechanisms depending on the cooling rate used in the ternary system. This may be due to the high supersaturation which accords with the high cooling rate resulting in a metastable form of nucleus formed in the beginning. As the supersaturation is decreased, the unstable form of the crystals tends to form a more stable form, which causes the secondary nucleation.⁴⁶ Another possible reason is morphologic transformation. Needle-like crystals could be observed by the naked eye initially at high cooling rates, but hexagonal prisms were found through SEM (Figure 2) at the end of the experiments.

4.4. Induction Time Analysis. Results obtained using the induction time method are shown in Figure 9. Experiment 40–0.4 exhibits a linear relationship over the whole range of cooling

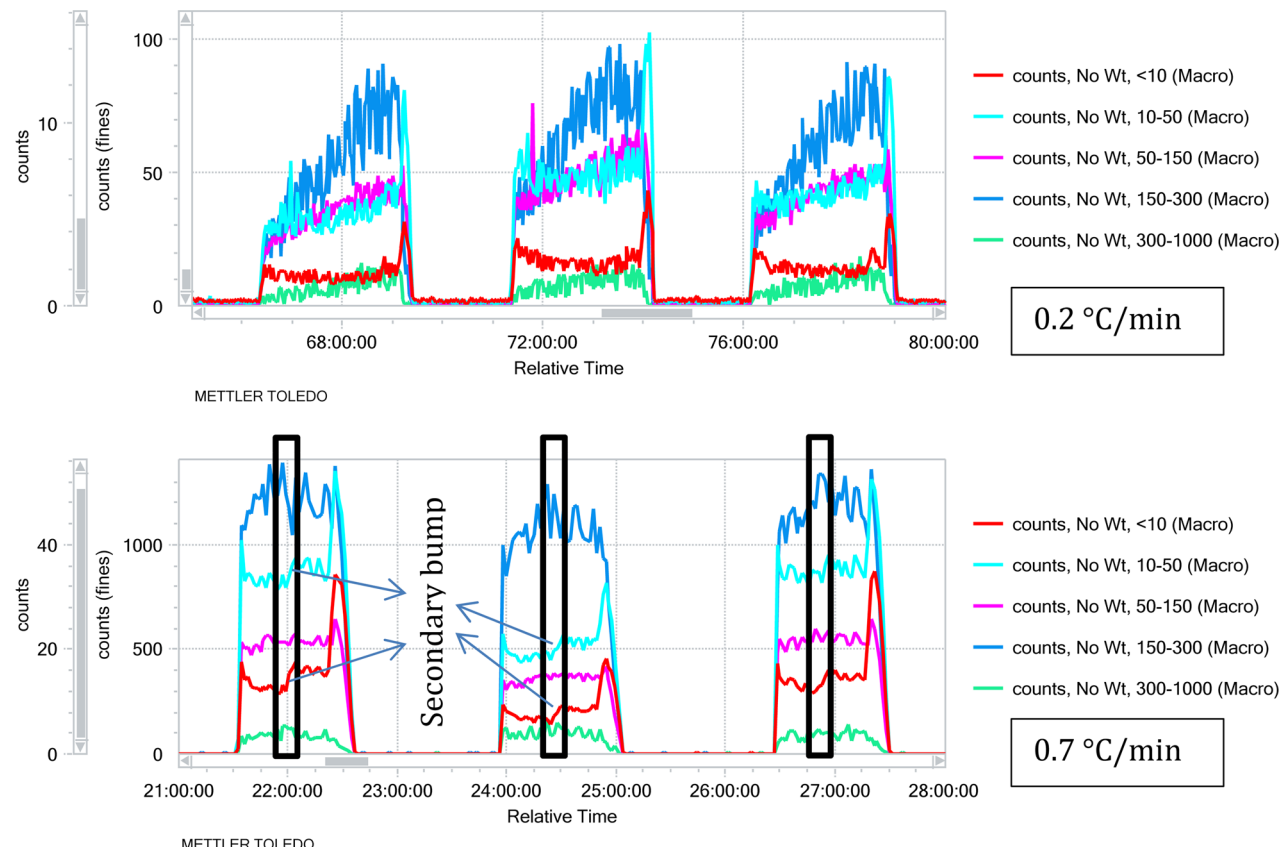


Figure 8. FBRM data on experiment 40–0.3 with different cooling rates (0.2 °C/min and 0.7 °C/min).

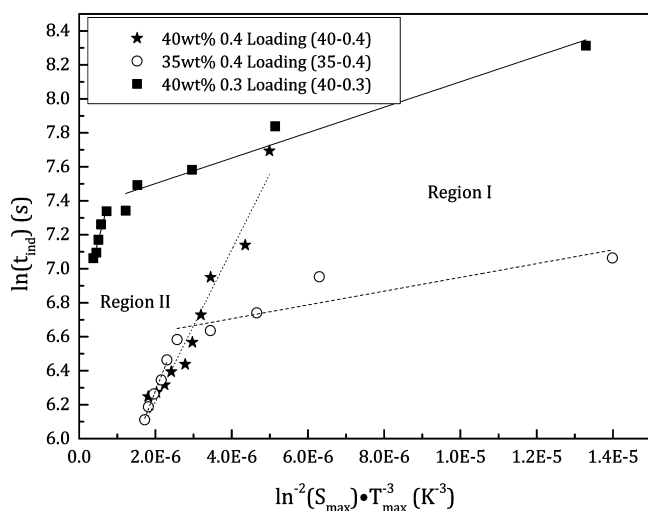


Figure 9. Relationship between induction time and supersaturation using induction time method.

rates investigated. This is similar to the trend found using Sangwal's CNT method. Results from experiments 35–0.4 and 40–0.3 were divided into two linear regions, which were also consistent with the results from Sangwal's method (Figure 7). This division may also be found in others' works.^{18,23,47} Both methods indicate that two nucleation mechanisms coexist. The nucleation kinetics parameters evaluated based on this method are presented in Table 5.

The results show that with increasing cooling rate (the decrease of $\ln^{-2}(S_{\text{max}})$), the solid–liquid interfacial energy γ_{eff} increases, which means the energy barrier for nucleation increases. It becomes difficult for precipitation, and hence the relationship between induction time ($\ln(t_{\text{ind}})$) and supersaturation ($\ln^{-2}(S_{\text{max}})$) has a greater slope. This may be due to the strong interaction between K_2CO_3 and KHCO_3 . However, the supersaturation also increased with increasing cooling rates. Therefore, there is a trade-off between ionic interactions and supersaturation when cooling the solution. Moreover, the surface entropy factor f_s which determines crystal growth mechanisms may be calculated using eq 26;⁴⁸ the results are also shown in Table 5.

Table 5. Nucleation Kinetics Parameters Obtained Using Induction Time Method

exp. group	region	slope ($\times 10^{-5}$)	intercept	R^2	A ($\#\text{-m}^{-3}\text{·s}^{-1}; \times 10^3$)	r_{eff} ($\times 10^3$ J/mol)	f_s
40–0.4		4.47	5.32	0.95	4.88	2.29	0.347
35–0.4	I	0.749	7.35	0.95	0.641	1.26	0.205
	II	8.66	6.73	0.95	2.85	2.85	0.463
40–0.3	I	0.405	6.54	0.75	1.03	1.03	0.164
	II	5.74	5.13	0.98	2.49	2.49	0.397

$$f_s = \frac{4\Omega^{2/3}\gamma_{\text{eff}}}{\kappa_B T_{\max}} \quad (26)$$

The value of the surface entropy factor f_s represents the roughness of the interfacial surface. The small value of f_s results from a rough interfacial surface. If the value of f_s is less than 3, the crystals follow continuous growth, and if f_s is between 3 and 5, the crystals follow two-dimensional growth (BCF model). If f_s is above 5, spiral growth or screw dislocation is expected, and the growth rate is very slow.⁴⁸ The value of f_s in all experiments in this study is less than 3, indicating that the roughness of the KHCO₃ interfacial surface is significantly large, and thus the crystals may follow a continuous growth mechanism. This can also be justified from SEM images, which are shown in Figure 10. Initially, the crystal surface of the KHCO₃ precipitate is

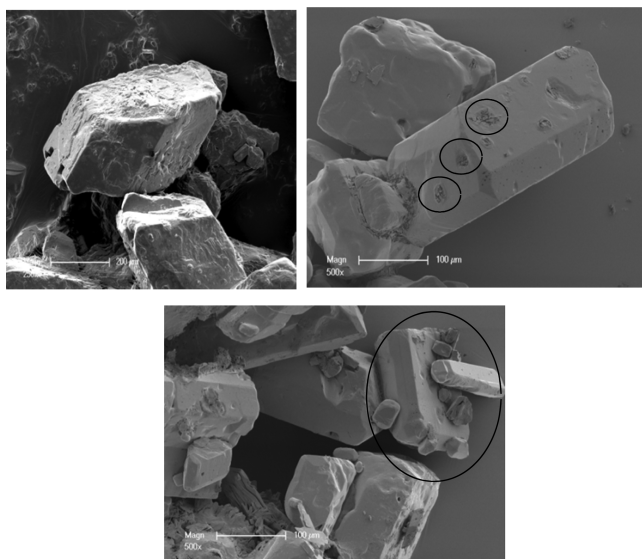


Figure 10. SEM of crystal interfacial surface. The circles indicate irregular protrusions on the surface of the bicarbonate crystals.

significantly rough, which provides sufficient spots for KHCO₃ to be embedded. Redislocation of this material is difficult due to the low energy barriers, and thus γ_{eff} is low. The rough surface is filled continuously by the new material, and the crystals grow until their surface becomes smooth.

After this, there were some irregular shaped protrusions (circles shown in Figure 10) on the surface, these sites provided further favorable locations or steps for crystal growth and particle deposition. Fine particles adhered onto these protrusions and integrated together with the main surface. This agreed with Hou's work⁴⁹ but cannot be explained by f_s value.

5. CONCLUSION

The primary nucleation kinetics of the concentrated K₂CO₃–KHCO₃–H₂O ternary system were investigated in FBRM and with an Optimax workstation. Kalicinite, KHCO₃, was confirmed as the only precipitate in the system, and a regressed ENRTL model using Aspen Plus was validated for predicting the solubility of the ternary system and used for evaluating nucleation kinetics. The MSZW method including the Nývlt approach, self-consistent Nývlt approach, and Sangwal's CNT approach and pseudoinduction time method were applied to assess the nucleation kinetics. All methods resulted in linear

relationships, and their nucleation kinetics could be determined. Sangwal's CNT approach provided consistent results with the induction time method, where two divided regions and nucleation mechanisms were discovered in the system. However, the growth of the nucleus to a detectable size was assumed negligible when applying both methods. Additionally, secondary nucleation may occur at high supersaturation and needs to be considered. Therefore, a more advanced model relating to particle size distribution using population balance should be developed to evaluate nucleation kinetics and growth kinetics simultaneously in further work.

■ AUTHOR INFORMATION

Corresponding Author

*Tel.: +61 3 83440048. Fax: +61 3 83444153. E-mail: mumfordk@unimelb.edu.au.

ORCID

Guoping Hu: 0000-0002-7480-8411

Kathryn H. Smith: 0000-0003-2060-9369

Geoffery W. Stevens: 0000-0002-5788-4682

Kathryn A. Mumford: 0000-0002-7056-5600

Notes

The authors declare no competing financial interest.

■ ACKNOWLEDGMENTS

The authors gratefully appreciate the financial and technical support from the Peter Cook Centre for CCS Research and assistance from the Particulate Fluids Processing Centre (PFPC), a special research centre of the Australian Research Council.

■ REFERENCES

- (1) Kothandaraman, A. *Carbon* **2010**, 144–184.
- (2) Mumford, K. A.; Wu, Y.; Smith, K. H.; Stevens, G. W. *Front. Chem. Sci. Eng.* **2015**, 9 (2), 125–141.
- (3) Thee, H.; Nicholas, N. J.; Smith, K. H.; da Silva, G.; Kentish, S. E.; Stevens, G. W. *Int. J. Greenhouse Gas Control* **2014**, 20, 212–222.
- (4) Shen, S.; Feng, X.; Zhao, R.; Ghosh, U. K.; Chen, A. *Chem. Eng. J.* **2013**, 222, 478–487.
- (5) Nejad, T.; Borhani, G.; Akbari, V.; Afkhamipour, M.; Kamaruddin, M.; Hamid, A.; Manan, Z. A. Comparison of equilibrium and non-equilibrium models of a tray column for post-combustion CO₂ capture using DEA-promoted potassium carbonate solution. *Chem. Eng. Sci.* **2015**, 122, 291–298.
- (6) Hu, G.; Nicholas, N. J.; Smith, K. H.; Mumford, K. A.; Kentish, S. E.; Stevens, G. W. *Int. J. Greenhouse Gas Control* **2016**, 53, 28–40.
- (7) Smith, K.; Lee, A.; Mumford, K.; Li, S.; Indrawan; Thanumurthy, N.; Temple, N.; Anderson, C.; Hooper, B.; Kentish, S.; Stevens, G. Pilot plant results for a precipitating potassium carbonate solvent absorption process promoted with glycine for enhanced CO₂ capture. *Fuel Process. Technol.* **2015**, 135, 60–65.
- (8) Smith, K.; Xiao, G.; Mumford, K.; Gouw, J.; Indrawan, I.; Thanumurthy, N.; Quyn, D.; Cuthbertson, R.; Rayer, A.; Nicholas, N.; Lee, A.; Da Silva, G.; Kentish, S.; Harkin, T.; Qader, A.; Anderson, C.; Hooper, B.; Stevens, G. *Energy Fuels* **2014**, 28 (1), 299–306.
- (9) Marciak, B. *J. Cryst. Growth* **2002**, 236, 347–356.
- (10) Parsons, A. R.; Black, S. N.; Colling, R. *Automated Measurement of Metastable Zones for Pharmaceutical Compounds*; Elsevier: Amsterdam, 2003; Vol. 81.
- (11) Zhang, Y.; Jiang, Y.; Zhang, D.; Qian, Y.; Wang, X. Z. *Chem. Eng. Res. Des.* **2015**, 95 (2), 187–194.
- (12) Titiz-Sargut, S.; Ulrich, J. *Chem. Eng. Process.* **2003**, 42 (11), 841–846.
- (13) Wu, S.; Feng, F.; Zhou, L.; Gong, J. *J. Cryst. Growth* **2012**, 354, 164–168.

- (14) Nagy, Z. K.; Fevotte, G.; Kramer, H.; Simon, L. L. *Chem. Eng. Res. Des.* **2013**, *91*, 1903–1922.
- (15) Brown, C. J.; Ni, X.-W. *CrystEngComm* **2012**, *14* (8), 2944.
- (16) Nagy, Z. K.; Fujiwara, M.; Woo, X. Y.; Braatz, R. D. *Ind. Eng. Chem. Res.* **2008**, *47* (4), 1245–1252.
- (17) Kee, N. C. S.; Arendt, P. D.; May Goh, L.; Tan, R. B. H.; Braatz, R. D. *CrystEngComm* **2011**, *13* (4), 1197.
- (18) You, S.; Zhang, Y.; Zhang, Y. *J. Cryst. Growth* **2015**, *411*, 24–29.
- (19) Sun, X.; Sun, Y.; Yu, J. *J. Cryst. Growth* **2015**, *419*, 94–101.
- (20) Kadam, S. S.; Kulkarni, S. A.; Coloma Ribera, R.; Stankiewicz, A. I.; ter Horst, J. H.; Kramer, H. J. M. *Chem. Eng. Sci.* **2012**, *72*, 10–19.
- (21) Wang, L.-Y.; Zhu, L.; Yang, L.-B.; Wang, Y. F.; Sha, Z.-L.; Zhao, X.-Y. *J. Cryst. Growth* **2016**, *437*, 32–41.
- (22) Kubota, N. *J. Cryst. Growth* **2008**, *310* (3), 629–634.
- (23) Gherras, N.; Fevotte, G. *J. Cryst. Growth* **2012**, *342* (1), 88–98.
- (24) Mersmann, A. *Crystallization Technology Handbook*; Marcel Dekker: New York, 2001.
- (25) Nývlt, J. *J. Cryst. Growth* **1968**, *3*–4, 377–383.
- (26) Sangwal, K. *J. Cryst. Growth* **2011**, *318* (1), 103–109.
- (27) Sangwal, K. *Cryst. Res. Technol.* **2009**, *44* (3), 231–247.
- (28) Li, H. *Process Measurements and Kinetics of Unseeded Batch Cooling Crystallisation*; Georgia Institute of Technology: Atlanta, 2015.
- (29) Mullin, J. W. *Crystallization*; Butterworth-Heinemann: Boston, 2001.
- (30) Ling, Z.; Zhao, W.; Meijing, Z.; Mingxia, G.; Shijie, X.; Qiuxiang, Y. *Chin. J. Chem. Eng.* **2016**, *313*–318.
- (31) Zhao, X.; Smith, K. H.; Simioni, M. A.; Tao, W.; Kentish, S. E.; Fei, W.; Stevens, G. W. *Int. J. Greenhouse Gas Control* **2011**, *5*, 1163–1169.
- (32) Zhao, X.; Simioni, M. A.; Smith, K. H.; Kentish, S. E.; Fei, W.; Stevens, G. W. *Energy Fuels* **2009**, *23* (10), 4768–4773.
- (33) Tosh, J. S.; Field, J. H.; Benson, H. E.; Haynes, W. P. *Equilibrium Study of the System Potassium Carbonate, Potassium Bicarbonate, Carbon Dioxide, and Water*; U.S. Dept. of the Interior, Bureau of Mines: Washington, DC, 1959.
- (34) Wappel, D.; Joswig, S.; Khan, A. A.; Smith, K. H.; Kentish, S. E.; Shallcross, D. C.; Stevens, G. W. *Int. J. Greenhouse Gas Control* **2011**, *5* (6), 1454–1459.
- (35) Redman, T. P.; Smith, B. *A Guide to Scale-up of Batch Crystallisation from Lab to Plant: Real-Time Measurement of the Crystal Population*; Mettler Toledo: Columbus, OH, 2010.
- (36) Kadam, S. S.; Kramer, H. J. M.; ter Horst, J. H. *Cryst. Growth Des.* **2011**, *11* (4), 1271–1277.
- (37) Kezia, K.; Lee, J.; Zisu, B.; Weeks, M.; Chen, G.; Gras, S.; Kentish, S. *Water Res.* **2016**, *101*, 300–308.
- (38) Ye, Q.; Wang, X.; Lu, Y. *Chem. Eng. Res. Des.* **2015**, *93*, 136–147.
- (39) Lee, A.; Mumford, K. A.; Wu, Y.; Nicholas, N.; Stevens, G. W. *Int. J. Greenhouse Gas Control* **2016**, *47*, 303–309.
- (40) *Measurement of Crystal Growth and Nucleation Rates*; Inst. of Chemical Engineers: London, 2002.
- (41) Gilles, F.; Nesrine, G. *Cryst. Growth Des.* **2012**, *12* (7), 3407–3417.
- (42) Barrett, P.; Glennon, B. *Chem. Eng. Res. Des.* **2002**, *80* (7), 799–805.
- (43) Myerson, A. S. *Handbook of Industrial Crystallization*; Butterworth-Heinemann: Boston, 2002.
- (44) Sangwal, K. *CrystEngComm* **2011**, *13* (2), 489.
- (45) Sangwal, K. Novel Approach to Analyze Metastable Zone Width Determined by the Polythermal Method: Physical Interpretation of Various Parameters. *Cryst. Growth Des.* **2009**, *9*, 942–950.
- (46) Nagy, Z. K.; Fujiwara, M.; Woo, X. Y.; Braatz, R. D. *Ind. Eng. Chem. Res.* **2008**, *47* (4), 1245–1252.
- (47) Zhou, L.; Wang, Z.; Zhang, M.; Guo, M.; Xu, S.; Yin, Q. Determination of metastable zone and induction time of analgin for cooling crystallization. *Chin. J. Chem. Eng.* **2017**, *25*, 313–318.
- (48) Hao, H.; Wang, J.; Wang, Y. *J. Cryst. Growth* **2005**, *274* (3–4), 545–549.
- (49) Hou, J.; Wu, S.; Li, R.; Dong, W.; Gong, J. *Cryst. Res. Technol.* **2012**, *47* (8), 888–895.